ROYAL SOCIETY
OF CHEMISTRY

PAPER

Check for updates

Structure–property relationships for exciton polarons in organic–inorganic hybrid materials

Katherine A. Koch,†[a] Martin Gomez-Dominguez, [ID]†[b] Esteban Rojas-Gatjens, [ID][c] Alexander Evju,[a] K. Burak Ucer, [ID][a] Juan-Pablo Correa-Baena [ID]*[b] and Ajay Ram Srimath Kandada [ID]*[a]

By combining materials chemistry to fine-tune crystallographic features with coherent nonlinear spectroscopy, we systematically explore how organic–inorganic interactions affect polaronic coupling in two-dimensional (2D) hybrid semiconductors. We focus on layered metal halide perovskite derivatives (2D-MHPs) in which the photoexcitations manifest as exciton–polarons—coulombically bound electron–hole pairs dressed by lattice vibrations. To address the current lack of quantitative frameworks for characterizing exciton–lattice coupling, we employ resonant impulsive stimulated Raman scattering (RISRS) and nonlinear spectroscopy to accurately determine the Huang–Rhys parameter, a direct measure of lattice displacement induced by exciton–phonon interactions. Our results reveal a clear correlation between polaronic displacement and octahedral lattice distortion, with stronger polaronic coupling emerging from greater distortion induced by organic cation modification. This establishes a robust design principle for enhancing exciton–lattice interactions through targeted chemical engineering. Furthermore, we demonstrate that these structural modifications enable precise control over absorption lineshapes and significantly improve excitonic quantum coherence. These findings pave the way for the development of advanced optoelectronic devices, coherent light sources, and quantum emission technologies, offering a strategic framework for the rational design of next-generation hybrid semiconductor materials.

1. Introduction

Engineering the coupling between electronic excitations and lattice vibrations is crucial for optimizing the electronic, optical, and thermal properties of materials. This coupling significantly influences key optoelectronic parameters, including carrier mobility,[1–4] thermal conductivity,[5–8] optical absorption coefficients,[9–12] luminescence quantum yields,[13–15] and exciton binding energies.[9,16–18] Furthermore, the interplay between charge carriers and lattice fluctuations can give rise to emergent phenomena relevant to quantum technologies, while simultaneously disrupting quantum coherence by opening multiple scattering pathways.[19–25] Therefore, tailoring electron–phonon coupling is imperative to achieve the desired material functionality for specific applications.

Polaronic effects are significant in polar semiconductors, where they strongly influence electronic and optical properties.[26–29] As a charge carrier moves through a polar crystal, it distorts the surrounding lattice *via* electrostatic interactions, forming a coupled entity known as a polaron.[30,31] The strength of this coupling is often described by the dimensionless parameter α, estimated using the known values of the phonon energy and the dielectric response function.[32] Alternatively, it can be inferred from carrier effective mass enhancements[33–35] or optical signatures like vibronic replicas and vibrational lineshapes.[36–39]

In nanostructured material systems, electronic dynamics are often governed by Coulomb interactions between electrons and holes, forming bound pairs known as excitons.[40–42] Consequently, exciton–phonon coupling becomes a more relevant consideration. Although excitons are charge-neutral, the inherent and distinct lattice coupling of the constituent electrons and holes can still lead to substantial exciton–phonon interactions. In materials like III–V semiconductors with large Bohr radii, excitons interact with long-range optical phonons.[43–45] Conversely, in systems with localized excitons (*e.g.*, organic semiconductors), coupling to high-frequency molecular vibrations arises from local atomic reorganization and is described

[a] *Department of Physics & Center for Functional Materials, Wake Forest University, Winston-Salem, North Carolina 27109, USA. E-mail: srimatar@wfu.edu*

[b] *School of Materials Science and Engineering, Georgia Institute of Technology, 771 Ferst Dr NW, Atlanta, GA 30332, USA. E-mail: jpcorrea@gatech.edu*

[c] *School of Chemistry and Biochemistry, Georgia Institute of Technology, 771 Ferst Dr NW, Atlanta, GA 30332, USA*

† These authors contributed equally.

by Huang–Rhys factors.[46–48] Some organic–inorganic hybrid materials, notably 2D metal halides, exhibit unusually strong coupling between tightly bound excitons and low-energy lattice phonons.[49–53] In these systems, excitations are confined to quasi-2D layers of metal halide octahedra separated by organic cations.[54–56] Previous work suggests this behavior may stem from a complex interplay of long- and short-range exciton–phonon interactions mediated by organic–inorganic coupling,[57] though this mechanism remains to be substantiated.

Despite extensive studies over the past decade,[57–61] the mechanisms of exciton–lattice coupling and polaronic effects in hybrid materials remain unresolved. The influence of organic cations – positioned between metal halide octahedra and interacting *via* hydrogen bonds with halogens – is particularly unclear.[62,63] These cations induce local strain and distortions, altering octahedral angles and introducing static lattice disorder,[64–66] with implications for electronic structure, bandgap, and exciton binding energy.[67–70] However, their impact on phonon energies and exciton–phonon or polaronic interactions remains underexplored. Since cation substitution affects both lattice and electronic properties,[71–73] disentangling these effects is challenging and highlights the need to preserve exciton integrity in such investigations.

To explore these complex exciton–lattice interactions, we focus on a prototypical 2D metal halide perovskite (2D-MHP), $(PEA)_2PbI_4$, and its halogenated derivatives, $(F/Cl–PEA)_2PbI_4$. $(PEA)_2PbI_4$ serves as an ideal model due to its rich excitonic fine structure—four peaks spaced by $\delta \approx$ 35–40 meV—and strong exciton–phonon coupling.[57] RISRS measurements have revealed exciton-specific lattice reorganizations, confirming their polaronic nature.[59,74] Building on this, we systematically vary the organic cation to probe how structural changes influence polaronic coupling. Crystallography and linear spectroscopy provide sufficient evidence that the excitonic landscape remains largely intact across the three variations, allowing us to only comment on changes concerning the organic–inorganic framework as a whole. Utilizing RISRS, we establish that the organic cation influences the nature of coupling between the exciton and local lattice vibrations, directly impacting the polaronic character of the excitons. Our findings indicate that a systematic substitution of the organic cation could provide researchers a control knob to tune the complicated fine structure present and mitigate many-body scattering effects in these materials by altering the degree of polaronic coupling.

2. Experimental section

2.1. Sample preparation

Glass slides were cleaned using sequential ultrasonic baths of acetone and isopropanol (IPA) for 15 minutes each, followed by nitrogen drying and UV-ozone treatment for 15 minutes. The perovskite precursor solutions were prepared by dissolving equimolar amounts of PbI_2 (purity > 99.99%) and the corresponding organic cation [phenethylammonium iodide (purity > 99.99%), 4F-phenethylammonium iodide (purity > 99.99%)],

4Cl-phenethylammonium iodide (purity > 99.99%) in *N*,*N*-dimethylformamide (purity > 99.98%) at a concentration of 0.13 M. After stirring overnight, the perovskite films were deposited by dispensing 80 μL of the precursor solution onto the 2.54 cm^2 clean glass slide, then spin-coated at 6000 rpm for 30 s with an acceleration of 6000 rpm. Immediately after deposition, the films were thermally annealed at 100 °C for 10 minutes.

2.2. X-ray diffraction

XRD measurements were performed at Georgia Tech in the Institute for Electronics and Nanotechnology facilities. Measurements were taken under ambient conditions on the Rigaku Smartlab XE with Bragg–Brentano geometry using a CuKα source. The 2D perovskite films for X-ray diffraction were fabricated on soda lime glass.

2.3. Ultrafast transient absorption spectroscopy

Transient absorption spectroscopy measurements were performed using a pulsed femtosecond laser (Pharos Model PH1-20-0200-02-12, Light Conversion) emitting 1030 nm pulses at 1 kHz with a pulse duration of ~200 fs. The 2.88 eV pump beam, with a corresponding fluence of 50.9 μJ cm^{-2}, was generated by feeding half of the laser output to a commercial optical parametric amplifier (Orpheus, Light Conversion) while 5 mW was focused onto a sapphire crystal to obtain a single filament white-light continuum covering the spectral range 450–800 nm for the probe beam. The probe beam transmitted through the sample was detected by a high speed camera (FLC 3030, EB Stressing) in combination with a high resolution spectrometer (SpectraPro SP-2150, Princeton Instruments). All measurements were carried out in a vibration-free closed-cycle cryostation (Montana Instruments).

2.4. Two-dimensional coherent electronic spectroscopy

We employed 2D spectroscopy on $(F–PEA)_2PbI_4$ using the previously implemented scheme,[74,75] developed and described in detail by Turner and coworkers.[76] The pulses used for these measurements were generated by a home-built single pass non-collinear optical parametric amplifier pumped by the third harmonic of a Yb:KGW ultrafast laser system (Pharos Model PH1-20-0200-02-10, Light Conversion) emitting 1030 nm pulses at 100 kHz, with an output power of 20 W and pulse duration of 220 fs. The pulses were individually compressed using a home-built implementation of a pulse shaper using a chirp scan.[77] The resulting pulse duration was 25 fs full-width at half-maximum (FWHM), as measured by second-harmonic generation cross-frequency-resolved optical gating (SHG-XFROG). All measurements were carried out in a vibration-free closed-cycle cryostat (Montana Instruments).

3. Results and discussion

It is well established that the choice of organic cation influences both the lattice parameters and electronic structure.[67,68,78]

This journal is © The Royal Society of Chemistry 2025

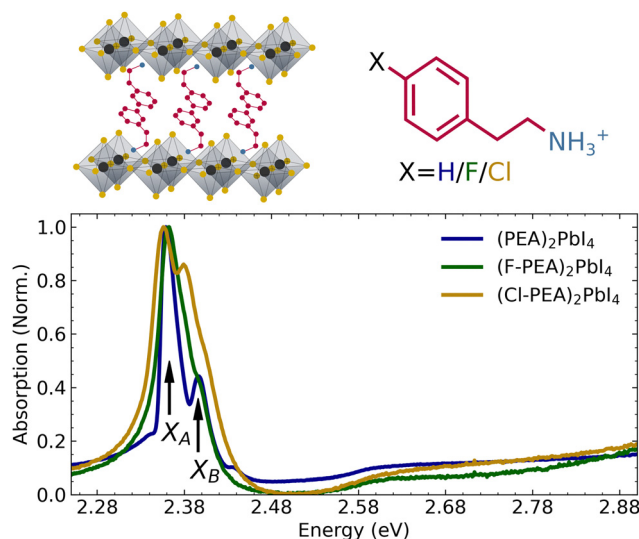*J. Mater. Chem. C*, 2025, **13**, 23416–23426 | **23417**

Fig. 1 (top) Structure schematic of the material system and the chemical structure of the PEA organic cation and the halogenated cations. (bottom) Linear absorption spectra at 15 K for all three materials.

In this study, we selected three cations—unsubstituted phenethylammonium (4-H), fluorine-substituted phenethylammonium at the fourth position (4-F), and chlorine-substituted phenethylammonium at the fourth position (4-Cl)—to minimize disruption to the lead-halide octahedral framework (Fig. 1). This approach ensures that the electronic structure and excitonic characteristics remain largely unaffected, allowing us to isolate and observe differences due to the organic–inorganic interactions as a whole. Indeed, as shown in Fig. 1, the linear absorption spectra of all samples exhibit qualitatively similar features, with the primary exciton peak and carrier continuum edge appearing at the same energy position. However, we observe discernible differences in the exciton fine structure among the samples. For the sake of convenience, we label the dominant exciton peaks as X_A and X_B, and it can be seen that the relative intensities of the two peaks vary with the organic cation substitution.

The X-ray diffraction patterns measured from the 2D MHP thin films used in this work are shown in Fig. 2(c). These materials exhibit a preferred out-of-plane orientation, as indicated by the characteristic Bragg peaks corresponding to the {002} family of planes.[79,80] All the materials form oriented Ruddlesden–Popper phases with varying interplanar distances, as evident from the spacing between the {002} planes. Among the samples, $(Cl–PEA)_2PbI_4$ exhibits the greatest interplanar distance, while $(PEA)_2PbI_4$ has the smallest. The diffraction patterns obtained for the thin films correlate well with previously reported single-crystal X-ray diffraction,[81] as shown by the comparison between Fig. 2(c) and Fig. S1. The experimentally measured thin-film XRD closely aligns with the simulated diffractogram for the $\langle 001 \rangle$ facet orientation, obtained from the single-crystalline data available in the literature.[81] Furthermore, the linear response of our thin films, as can be seen by the photoluminescence (PL) spectra in

Fig. S2, is not significantly different from that of the single crystal data found in ref. 82.

To further explore the structural differences induced using different cations, we focus on two parameters that are relevant for the electronic properties: equatorial distortion and bond angle variance, illustrated schematically in Fig. 2(a). Additional structural parameters, such as the quadratic elongation (λ), distortion index (D), and the effective coordination number (ECoN), were also explored, and more details can be found in the SI (Section S2). The electronic structure and bandgap are particularly sensitive to equatorial distortion,[78] which, as shown in Fig. 2(b), remains largely consistent across the three samples studied. Although we do not have direct measurements of the electron and hole effective masses, the consistency of the equilateral distortion angle suggests no significant change in the electronic properties. Hence, the crystallography work aligns with the linear absorption data in Fig. 1, which suggests similar exciton and bandgap energies across the samples.

To quantify angular distortions within the lead–iodide octahedra, we calculate the bond angle variance (σ^2), schematically represented in Fig. 2(a), which captures deviations from the ideal 90° bond angles. This metric, commonly used to assess octahedral distortion in low-dimensional perovskites,[83,84] is defined as:

$$\sigma^2 = \frac{1}{m-1}\sum_{i=1}^{m}(\phi_i - \phi_0)^2 \qquad (1)$$

where ϕ_i is the ith bond angle and ϕ_0 is the ideal bond angle for a regular octahedra (90°), which are estimated from the crystallographic data. Because σ^2 sums the squared deviations of all bond angles, even a modest change in σ^2 corresponds to a large, cumulative octahedral distortion. Fig. 2(d) shows the bond angle variance estimated for the three samples. The F-substituted cation $(F–PEA)_2PbI_4$ exhibits the greatest octahedral distortion, followed by $(PEA)_2PbI_4$ and then $(Cl–PEA)_2PbI_4$, which shows the least distortion. Although the implications of such distortions in 2D perovskites are still emerging, prior studies suggest that enhanced octahedral disorder may strengthen exciton–lattice coupling.[85–87] We return to the impact of these distortions in the Discussion section.

To investigate the impact of cation substitution on the motion of the metal-halide sublattice—specifically, the vibrational modes that couple directly with the exciton—we performed resonant impulsive stimulated Raman scattering (RISRS) measurements on $(PEA)_2PbI_4$ and its halogenated derivatives, $(F–PEA)_2PbI_4$ and $(Cl–PEA)_2PbI_4$. In this technique, an ultrashort optical pulse impulsively excites the lattice, generating a coherent vibrational wavepacket—a collective superposition of all Raman-active vibrational modes. This wavepacket then oscillates along the potential energy surfaces of both the ground and excited electronic states, following the vibrational coordinates defined by the coupled phonon modes.

The resulting modulation of the complex dielectric permittivity function, see Fig. 3(b), manifests as a time-dependent oscillatory signal in the differential transmission spectrum
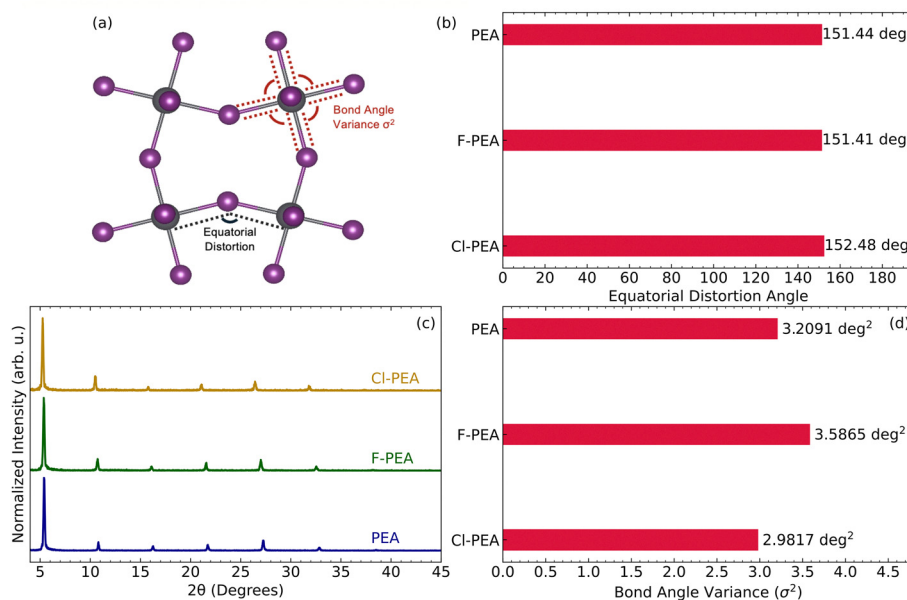
23418 | *J. Mater. Chem. C*, 2025, **13**, 23416–23426

This journal is © The Royal Society of Chemistry 2025

Fig. 2 (a) Pictorial depiction of the equatorial distortion angle and the bond angle variance (σ^2) as a measure of deviation from the ideal bond angle of 90°. Graphical representations of (b) the equatorial distortion angle, (c) the experimentally measured XRD patterns, and (d) the bond angle variance (σ^2) are shown for all three cations.
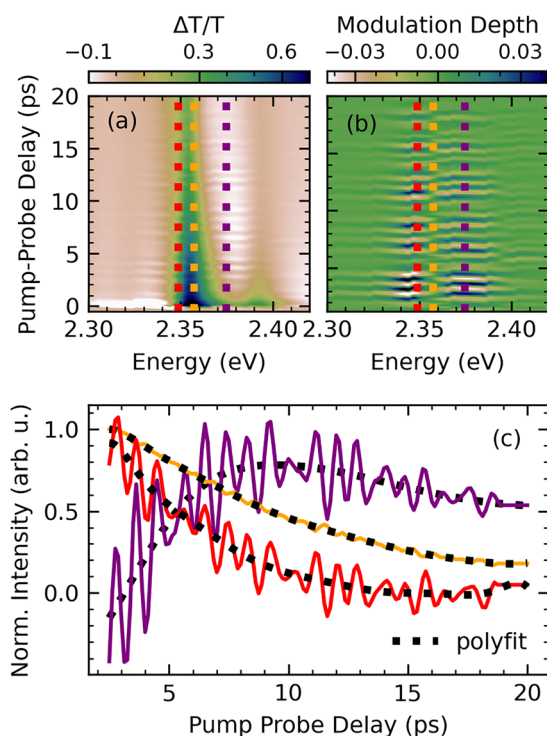

Fig. 3 (a) Differential transmission spectra and (b) coherent phonon oscillations of $(PEA)_2PbI_4$. (c) Spectral cuts of the differential transmission data to reveal experimental dynamics at three probe energies and their corresponding polynomial fits. It can be seen that the main exciton peak (yellow) experiences no oscillatory features in the raw differential transmission spectra. This energy corresponds to the node observed in the modulation spectra, see Fig. 4(g)–(i).

(Fig. 3(a)). To obtain this response, the electronic dynamics are subtracted from the differential transmission spectra using a high-order polynomial fit (17th-order), see Fig. 3(c). By performing a Fourier transform along the time axis in Fig. 3(b), we extract the RISRS modulation maps, shown in Fig. 4(a), (c) and (e). It is important to note that the transmission modulations induced by the coherent phonons appear exclusively at specific probe wavelengths, exhibiting a distinct lineshape. The nature and implications of these lineshapes will be discussed in detail later in this manuscript. The raw data for all three samples is shown in Fig. S4, and a more detailed description of how the RISRS data is obtained can be found in Sections S3 and S4 in the SI.

Focusing exclusively on $(PEA)_2PbI_4$, we can draw key insights from the beating map displayed in Fig. 4(a). In this figure, the black line represents the absorption spectrum, providing a reference for the excitonic resonances. Notably, the lower-energy exciton (X_A) exhibits a more pronounced modulation due to phonon interactions compared to the higher-energy exciton (X_B). This is evident from the characteristic dip in the modulation amplitude observed at the energy of X_A, signaling stronger exciton–phonon coupling at this resonance.

To further analyze the phonon contributions, we integrate the data over the energy axis, yielding the Raman spectra shown in Fig. 4(b). The RISRS spectrum reveals the presence of at least four distinct phonon modes. The data for $(PEA)_2PbI_4$ obtained in this study aligns well with previously reported Raman spectra from Thouin *et al.*[59] In that work, we demonstrated that different excitons drive distinct lattice reorganizations, thereby providing direct experimental evidence of their polaronic nature. That study, supported by density functional theory (DFT) calculations, established that all identified phonon modes below 10 meV in $(PEA)_2PbI_4$ originate from vibrations within the lead–iodide octahedral network.
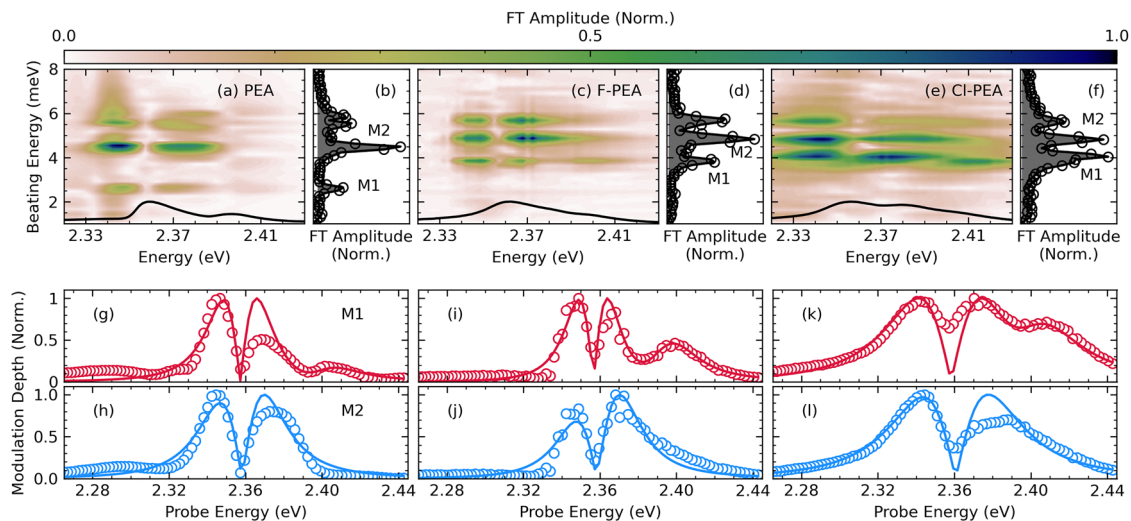
Fig. 4 Linear absorption (black line) and beating spectra as a function of detection energies for (a) $(PEA)_2PbI_4$, (c) $(F-PEA)_2PbI_4$, and (e) $(Cl-PEA)_2PbI_4$. Probe-energy-integrated vibrational spectra for (b) $(PEA)_2PbI_4$, (d) $(F-PEA)_2PbI_4$, (f) $(Cl-PEA)_2PbI_4$ respectively. All measurements were taken at 15 K. The corresponding spectral cuts of RISRS beating map and fitting results using eqn (2) and (3). This figure shows the modulation depth for phonon mode 1 (M1) and phonon mode 2 (M2), where spectral cuts were taken at (g) 2.3–2.9 meV and (h) 4.1–4.8 meV for $(PEA)_2PbI_4$, (i) 3.6–4.1 meV and (j) 4.5–5.3 meV for $(F-PEA)_2PbI_4$, (k) 3.6–4.4 meV and (l) 4.6–5.2 meV $(Cl-PEA)_2PbI_4$. The data is represented with open circles and the fit is the solid line.

We observe phonon modes within a similar energy range across all samples, as evident in the integrated RISRS spectra shown in Fig. 4(d) and (f). Given the energy range of these spectral modes, we attribute the observed phonons to the motion of the PbI_4^{2-} framework. Interestingly, although the inorganic sub-lattice remains largely intact across the different derivatives, distinct variations in the RISRS response are apparent. A particularly notable trend across both $(PEA)_2PbI_4$ derivatives is the blue shift of the lowest-energy phonon, accompanied by an increase in its intensity as we move from the $(F-PEA)_2PbI_4$ compound to $(Cl-PEA)_2PbI_4$. At present, crystallographic analysis and standard *ab initio* density functional theory (DFT) have not provided clear evidence for a specific structural variable responsible for the observed phonon shifts, so their origin remains an open question. It is possible that more advanced computational approaches combined with refined structural models of layered perovskites could provide additional insight into the mechanism behind the shift, but that is beyond the scope of this work. For the sake of further discussion in this manuscript, we label the dominant modes as M1 and M2, which have different energies in each material, tabulated in Table 1.

Beyond changes in the eigenmode energies, we now examine how the RISRS response evolves across different probe energies. Vertical cuts along the beating energy axis of the probe-energy-resolved beating maps in Fig. 4(a), (c) and (e) exhibit a characteristic lineshape. Notably, at the exciton absorption peak energy, a distinct dip appears in the modulation spectrum. The observed dual-peak lineshape and π phase shift at the peak energy (see Fig. S6) are hallmarks of vibrational wavepacket dynamics, where the exciton energy is modulated by the motion of a vibrational wavepacket along a real-space vibrational coordinate associated with the coherently excited phonon.[30,39] This characteristic spectral feature is typically seen in localized electronic excitations of organic chromophores coupled to molecular vibrations.[88–95] Similar spectral responses have been reported in 2D metal halides like $(PEA)_2PbI_4$ and its derivatives, which have been interpreted—both by us[59] and others[58,60]—as signatures of polaronic coupling between excitons and lattice phonons. As a consequence, the photoexcitations must be described as exciton–polarons, wherein the Coulomb correlations of electron–hole pairs are renormalized by lattice dynamics *via* polaronic effects. Within this framework, the lattice reorganizes along the vibrational coordinates defined by the lattice phonons in the presence of excitons. The modulation strength and lineshape symmetry are linked to the extent of displacement in the excited-state PES and the degree of anharmonicity in the potential.

The RISRS maps in Fig. 4(a), (c) and (e) reveal that the modulation associated with M2 occurs exclusively at the energy of the dominant peak, X_A, in the linear absorption of all samples. In contrast, the modulation due to M1 appears not only at X_A but also at the higher-energy absorption peak, labeled X_B. This observation suggests the presence of two distinct excitonic states, X_A and X_B, each interacting uniquely with the lattice phonons M1 and M2, and with distinct lattice displacements (Fig. 5). To further quantify these differences across the samples, we analyze the modulation amplitude spectra, obtained through an integration over the beating energy axis of the RISRS map, for M1 and M2.

Table 1 Dominant phonon mode (M1 & M2) energies for $(PEA)_2PbI_4$, $(F-PEA)_2PbI_4$, and $(Cl-PEA)_2PbI_4$

Mode	PEA (meV)	F–PEA (meV)	Cl–PEA (meV)
M1	2.3–2.9	3.6–4.1	3.6–4.4
M2	4.1–4.8	4.5–5.3	4.6–5.2

23420 | *J. Mater. Chem. C*, 2025, **13**, 23416–23426

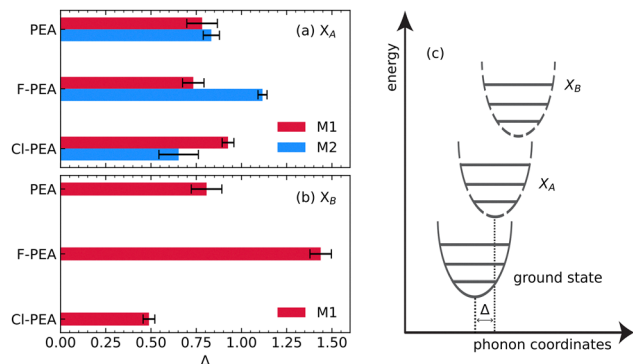This journal is © The Royal Society of Chemistry 2025

Fig. 5 The offset between the ground and excited state potential energy surfaces calculated from the Huang–Rhys fitting parameter for (a) exciton A (X_A) and (b) exciton B (X_B). (c) Schematic of potential energy surfaces, where the potential energy surfaces of X_A and X_B are composed of distinct vibrational manifolds.

The respective ranges of integration for each material are shown in Table 1.

Researchers have measured similar amplitude profiles due to vibrational wavepackets since the 1990s, but until recently, quantitative information has been difficult to extract.[96,97] Previously, the predominant approach for analyzing RISRS lineshapes was a quantum dynamics model proposed by Champion et al.,[98] which was employed in the earlier study on $(PEA)_2PbI_4$.[59] The Champion model is mathematically complex and requires a well-characterized linear absorption lineshape of the exciton as an input. The fitting process is also highly sensitive to the choice of lineshape function in the Elliott analysis, whether Lorentzian or secant-hyperbolic. Turner et al.,[99–101] developed a comparatively simple analytical model for femtosecond coherence spectra (FCS), which they define as the Fourier-domain amplitude and phase profiles, $A(\omega)$ and $\phi(\omega)$, respectively, as a function of detection frequency, ω, for a chosen oscillation frequency, ω_0. This model is more successful in reproducing asymmetry in the lineshape, and allows for more complicated applications that consider the inclusion of anharmonicity or unequal curvatures in the potential energy surfaces.[99] Moreover, it assumes that the duration of the optical pulse is in the impulsive regime for vibrational excitations, but not for electronic excitations, which is ideal for our experimental conditions. This model is based on the displaced harmonic oscillator framework, where both the ground and excited electronic states are harmonic potential energy surfaces of frequency ω_0, offset horizontally by a displacement Δ, which is directly related to the Huang–Rhys factor by $\mathbf{S} = \frac{1}{2}\Delta^2$, see Fig. 5(c). The vertical offset is represented by the exciton resonance energy ω_{eg}. A doorway-window approach is used, where the vibrational wavepacket oscillating within the excited state PES is projected onto the ground state PES, and the Frank–Condon wavefunction overlap is determined.[97,100]

The starting point of the model is the transient absorption data, $S(\omega, \tau_2)$, where τ_2 is the pump probe delay and ω is the probe (detection) energy axis. A Fourier transform over the time

interval results in a complex valued spectrum, $M(\omega, \omega_2) = \mathscr{F}[S(\omega, \tau_2)]$. The amplitude and phase profiles of a specific mode, with frequency ω_0, are functions of detection frequency (ω), and given by, $A(\omega) = M(\omega, \omega_2)|_{\omega_2=\omega_0}$. The two relevant equations for this model are:

$$M(\omega; \omega_0) = e^{-2\mathbf{S}} \sum_{n,m=0}^{\infty} m!\mathbf{S}^{2n+m+1} A_{n,m}(\mathbf{S})A_{n+1,m}(\mathbf{S})$$
$$\times \left[\frac{1}{\omega - \omega_{n+1,m} + i\gamma/2} - \frac{1}{\omega - \omega_{n,m} - i\gamma/2} \right] \quad (2)$$

where the auxiliary functions are given by:

$$A_{a,b}(\mathbf{S}) = \sum_{j=0}^{\min[a,b]} \frac{(-1)^j \mathbf{S}^{-j}}{j!(a-j)!(b-j)!} \quad (3)$$

In these expressions, m and n index the vibrational eigenstates of the ground and excited electronic states, respectively, where the vertical offset ω_{eg} is implicitly included in $\omega_{a,b} = (E_a - E_b)/\hbar$, and γ is the dephasing parameter. Physically eqn (2) and (3) represent that each FCS spectra is a collection of Lorentzian peaks, where each peak is broadened by γ and weighted by an auxiliary function, see Fig. 6. The fit parameters for this model are $\{\mathbf{S}, \gamma, \omega_{eg}\}$ where the phonon frequency, ω_0, is defined directly from the measured spectra. Value restrictions can be placed on both γ and ω_{eg} because they can be approximated from the linear absorption linewidths and the energy of the exciton resonance, respectively. This leaves the Huang–Rhys factor, $\mathbf{S} = \frac{1}{2}\Delta^2$, as the only true fitting parameter, where its value and associated error is an output of the fitting routine. The extracted Huang–Rhys parameter depends on the relative lineshape of the modulation spectra, rather than the absolute magnitude; thus, performing the fitting routine on normalized data does not impact the results. Additional details on how variations in the Huang–Rhys parameter impacts the
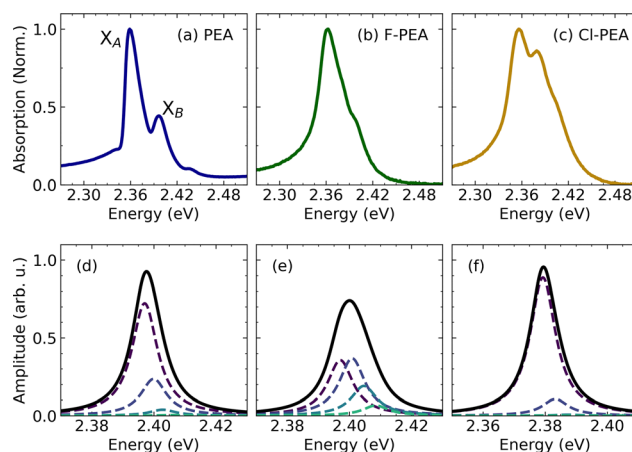

Fig. 6 Linear absorption spectrum of (a) $(PEA)PbI_4$, (b) $(F–PEA)PbI_4$, and (c) $(Cl–PEA)PbI_4$. (d)–(f) Represent the collection of Lorentzian peaks, weighted by $F_{n0} = \frac{e^{-\mathbf{S}}\mathbf{S}^n}{n!}$ where n denotes the vibrational transition, that make up the X_B resonance, and the sum of those peaks (black line).

This journal is © The Royal Society of Chemistry 2025

J. Mater. Chem. C, 2025, **13**, 23416–23426 | **23421**

modulation spectra are provided in Section S4 of the SI (see Fig. S7). These values were used to determine the displacement of the excited state PES, where $\Delta = \sqrt{2 \cdot S}$ and its corresponding error was determined through error propagation methods. Turner and co-workers introduced an expanded anharmonic model, which incorporates an additional fit parameter to account for an anharmonic potential energy surface. However, in our case, the harmonic model already provides reasonable agreement with the experimental data, as shown in Fig. 4(g)–(l). Therefore, we chose not to adopt the anharmonic extension as it would increase model complexity without offering a clear improvement in fit quality.

This model was able to reproduce the M2 modulation spectra of all three compounds shown in Fig. 4(h), (j) and (l), which follow the expected dual peak lineshape. However, as can be seen in Fig. 4(g), (i) and (k) the lowest energy phonon mode (red) deviates from the two-peak structure seen in the second mode (blue), and a third peak is emerging at higher energies. For these low energy phonon modes, we expanded the model to include two distinct excited state potential energy surfaces, each for X_A and X_B respectively, see eqn (4) and Fig. 5(c), where the relative weight of contribution for the X_A and X_B PESs were determined using the absorption spectrum (A = intensity of X_A resonance and B = intensity of X_B resonance).

$$M_{\text{total}}(\omega; \omega_0) = A \cdot M_{X_A} + B \cdot M_{X_B} \qquad (4)$$

This analytical model enabled the extraction of the Huang–Rhys parameter, which is related to the equilibrium offset between the ground and excited state potential energy surfaces, and hence the extent of polaronic coupling. We highlight that the FCS model is the most accurate estimation of the Huang–Rhys parameter because it provides direct access to time-resolved exciton–phonon dynamics, unlike Raman or sideband methods which infer the Huang–Rhys parameter through steady-sate or frequency domain data. Additionally, the FCS method addresses the fact that phonon replicas in the Raman or photoluminescence spectra are difficult to deconvolute, as it resolves the exciton–phonon interactions temporally, enabling one to distinguish phonon modes with femtosecond precision, which is necessary for these systems as the phonon energies of interest are below 10 meV. In Fig. 5(a) and (b), we show the Huang–Rhys parameter associated with the two dominant vibrational modes (M1 and M2) for two distinct excitonic resonances (labeled X_A and X_B) in the optical spectrum.

For all systems considered, the PES of X_A is displaced along coordinates associated with both M1 and M2, while X_B shifts exclusively along M1. We first look at the displacement Δ of X_A along the M1 coordinate, where $(F-PEA)_2PbI_4$ exhibits the least displacement and $(Cl-PEA)_2PbI_4$ shows the greatest, with the non-halogenated compound, $(PEA)_2PbI_4$, displaying an intermediate value. Interestingly, the displacement of X_A along the M2 mode, which has been identified as the dominant mode in the photoexcitation dynamics of the X_A exciton,[57,59] follows the opposite trend, albeit to a greater magnitude. Moreover, for X_B, which is displaced solely along M1, a similar trend to X_A and

M2 emerges, with $(F-PEA)_2PbI_4$ demonstrating the most significant phonon dressing and $(Cl-PEA)_2PbI_4$ demonstrating the least. Upon first glance, the trends of the displacement (Δ) are particularly interesting, especially when considering the Raman spectra. As noted earlier, there was a consistent blue shift in the low-energy phonon modes when moving from PEA to F–PEA and Cl–PEA, indicating that the observed trends in Δ cannot be due to phonon energy alone. If that were the case, one would expect PEA to exhibit the lowest Δ value and Cl–PEA to exhibit the largest, which, as shown in Fig. 5 is not true. On a related note, the displacement trends cannot be directly attributed to dielectric effects. While the dielectric constants and therefore the polarizabilities of the organic layers do vary with the substituted cations, (PEA < Cl–PEA < F–PEA), this ordering also does not align with the observed displacement trend.

A clear and striking correlation emerges between the trends in exciton–phonon coupling parameters shown in Fig. 5(b) and the crystallographic parameters, particularly the bond angle variance (BAV) in Fig. 2(d). In this instance, the BAV is an estimation of the degree of angular distortions that the lattice is capable of withstanding, serving as an approximation of the structural pliability of the material. When bond angles are close to their ideal values, the structure is more rigid and less susceptible to external stress or deformation. Conversely, a higher BAV indicates increased structural flexibility,[78,102,103] allowing the material to accommodate larger distortions induced by external forces. The lattice dressing effect in the presence of photocarriers, previously discussed as the polaronic effect, operates through Coulomb-mediated lattice deformations, which are directly linked to lattice flexibility. Our experimental results suggest that substituting PEA with F–PEA enhances the flexibility of the PbI_4^{2-} sub-lattice, influencing the lattice dressing of excitons. In contrast, substitution with the chlorinated compound leads to a more rigid sub-lattice. Notably, while the overall electronic structure remains largely unchanged across the samples, subtle local interactions are fine-tuned by organic cation substitution. These structural modifications have significant and observable effects on key spectral characteristics, which we will explore in the following. The complex spectral fine structure, characterized by multiple transitions at the exciton energy, has been widely reported in numerous 2D metal-halide perovskites (2D-MHPs) incorporating various organic cations and halogens.[29,56,104–106] However, the origin of this fine structure remains an open question, with ongoing debate as to whether the observed transitions correspond to distinct excitonic states or a single transition exhibiting vibronic progression.

In our previous work, we argued that each observed peak in absorption and photoluminescence (PL)—denoted here as X_A and X_B – corresponds to distinct excitonic states. However, we also noted the possible presence of additional peaks, obscured within the broad linewidths of the linear response, which may be attributed to phonon replicas. Indeed, analysis based on the displaced oscillator model, used to interpret the resonant inelastic scattering of Raman signals response, predicts the presence of phonon replicas in the optical spectra. These replicas

23422 | *J. Mater. Chem. C*, 2025, **13**, 23416–23426

This journal is © The Royal Society of Chemistry 2025

are separated by the characteristic phonon energies M1 and M2 and are weighted according to the estimated Huang–Rhys factors.

Notably, variations in the relative intensities and linewidths of the exciton fine structure can be observed across different samples (see Fig. 1 and 6(a)–(c)). Specifically, in $(F–PEA)_2PbI_4$, the relative strength of X_B appears quenched, whereas in $(Cl–PEA)_2PbI_4$, it is enhanced. To further investigate how lattice displacement influences the oscillator strength of the X_B resonance, we examine its underlying vibronic structure. Fig. 6(d)–(f) depict a collection of Lorentzian peaks weighted by the experimentally determined Franck–Condon factors, given by $F_{n0} = \dfrac{e^{-S}S^n}{n!}$, where n denotes the vibrational transition that makes up the X_B resonance. The black line represents the sum of these peaks. It is evident that an increase (decrease) in lattice displacement enhances (suppresses) the Franck–Condon overlap of higher-lying vibrational states, leading to a quenched (enhanced) transition. Thus, this suggests that organic cation substitution can offer effective ways of fine-tuning the spectral characteristics of the excitons in 2D-MHPs, which we have recently argues plays a critical role in enabling their application in polariton lasers.[20,107] To further substantiate these claims, a theoretical framework needs to be developed to continue studying the impact of the polaronic nature of these resonances.

Our findings further reinforce the hypothesis that photo-excitations in these materials must be understood within the exciton–polaron framework.[57] Operating within this same framework, Dyksik et al.[108] previously employed continuous-wave resonant Raman spectroscopy and the displaced harmonic oscillator model to estimate Huang–Rhys factors in $(PEA)_2PbI_4$. Through detailed analysis, they reported Huang–Rhys factors of approximately 7–8 for low-energy phonons (below 8 meV)—significantly larger than the values we have estimated above. While both approaches involve rigorous analysis, this discrepancy underscores the need for a deeper understanding of the methodologies and assumptions involved. We believe that our work will stimulate further investigation into the precision and limitations of experimental techniques used to extract such photophysical parameters, particularly in emerging hybrid materials. Furthermore, it may prompt the development of more refined theoretical models and critical evaluation of existing experimental interpretations.

The exciton–polaron framework becomes particularly relevant when considering many-body scattering effects. Within this framework, the exciton resides within a self-induced deformation cloud, where both phonon–phonon and exciton–phonon interactions contribute to the thermal dephasing of excitons. This dephasing manifests as a temperature-dependent increase in the homogeneous linewidth, γ. Previously, we noted that linear optical response is not an effective method to estimate γ,[105] necessitating the use of two-dimensional electronic spectroscopy $(2DES)^{74,76}$ instead. In ref. 74, we employed 2DES to study thermal dephasing in $(PEA)_2PbI_4$, allowing us to estimate the corresponding exciton–phonon interaction parameter. Importantly, we distinguish between the exciton–phonon

coupling parameters associated with lattice dressing and exciton scattering, as they stem from inherently different physical processes.

In this work, we extend our study to $(F–PEA)_2PbI_4$, applying 2DES to determine the temperature dependence of γ, where a detailed analysis of the experiment and linewidth analysis can be found in Sections S5 and S6 in the SI. By assuming that line broadening results from exciton scattering with a single thermally populated phonon mode, we fit γ to eqn (S3) to extract the effective energy (E_{LO}) of the scattered phonon and the effective interaction parameter (α_{LO}). The fitting result reveal an effective interaction parameter of $\alpha_{LO} = 1.58$ meV for $(F–PEA)_2PbI_4$ (see Fig. S9), which is significantly lower than the previously reported value of $\alpha_{LO} = 33$ meV for $(PEA)_2PbI_4$.[74]

Notably, when comparing both the exciton–phonon interaction and Huang–Rhys parameters of the two materials, we observe an inverse correlation: a higher Huang–Rhys parameter—indicative of stronger polaronic character—corresponds to a lower exciton scattering interaction parameter, indicating that our observations at 15 K are relevant for room temperature exciton interactions. This finding also highlights the interplay between polaron formation and exciton–phonon scattering in 2D-MHPs. These observations suggest that within the exciton–polaron framework, the dominant mechanism governing thermal dephasing is exciton–phonon scattering, rather than longitudinal optical (LO) phonons scattering with other LO phonons. Notably, in $(F–PEA)_2PbI_4$, the enhancement of polaronic character, coupled with a reduction in the interaction parameter, supports the previous hypothesis that lattice phonon dressing provides a protective effect for excitations.[57] A comparative analysis of the interaction and Huang–Rhys parameters for $(PEA)_2PbI_4$ and $(F–PEA)_2PbI_4$ suggests that stronger lattice dressing effectively shields the exciton, mitigating scattering effects. Although excessive distortion generally degrades performance, this polaronic protection mechanism presents an intriguing avenue for material scientists seeking to suppress many-body scattering effects, which is potentially useful in designing materials with enhanced optical coherence.

4. Conclusions

In summary, we have presented a comprehensive analysis detailing how exciton–phonon interactions are influenced by the organic cation, in 2D-MHP systems, specifically $(PEA)_2PbI_4$, $(F–PEA)_2PbI_4$, and $(Cl–PEA)_2PbI_4$. Linear spectroscopy and crystallography were utilized to confirm that the organic cation substitutions preserve the exciton landscape, while RISRS, crystallography, and the estimation of the Huang–Rhys parameter established that the organic cation and hence the degree of octahedral distortion influences the nature of coupling between the exciton and local lattice vibrations, directly impacting the polaronic nature of the excitons. It is evident from the analysis that careful engineering of the organic cation and the organic–inorganic interactions may offer a design route to control the degree of polaronic character of excitons, and

This journal is © The Royal Society of Chemistry 2025

J. Mater. Chem. C, 2025, **13**, 23416–23426 | **23423**

possibly provide an avenue to control the fine structure and weaken the many-body scattering effects of 2D-MHPs, which is crucial for advancements in material science.

Author contributions

KAK and MGD contributed equally to this work. KAK performed the RISRS measurements, analyzed the data, and wrote the manuscript under the supervision of ARSK. MGD fabricated the samples and performed the crystallography analysis under the supervision of JPCB. ERG and KAK performed 2D spectroscopy under the supervision of ARSK. KBU participated in the collection of the RISRS data, and AE contributed to the FCS analysis. The project was conceived and coordinated by ARSK.

Conflicts of interest

The authors declare no conflicts of interest.

Data availability

The data underlying this study are openly available in Zenodo at **https://doi.org/10.5281/zenodo.15352397**.

Supplementary information is available. See DOI: **https://doi.org/10.1039/d5tc02604k**.

Acknowledgements

References

1 C. Wehrenfennig, G. E. Eperon, M. B. Johnston, H. J. Snaith and L. M. Herz, *Adv. Mater.*, 2013, **26**, 1584.

2 H. T. Yi, X. Wu, X. Zhu and V. Podzorov, *Adv. Mater.*, 2016, **28**, 6509–6514.

3 L. Raimondo, L. Silvestri, A. Borghesi and S. Tavazzi, *J. Phys. Chem. C*, 2013, **117**, 26248–26254.

4 Y. Gong, S. Yue, Y. Liang, W. Du, T. Bian, C. Jiang, X. Bao, S. Zhang, M. Long, G. Zhou, J. Yin, S. Deng, Q. Zhang, B. Wu and X. Liu, *Nat. Commun.*, 2024, **15**, 1893.

5 Z. Tong, S. Li, X. Ruan and H. Bao, *Phys. Rev. B*, 2019, **100**, 144306.

6 J. Ordonez-Miranda, J. Alvarado-Gil and R. Yang, *J. Appl. Phys.*, 2011, **109**, 094310.

7 S.-X. Lin, X. Tan, H. Shao, J. Xu, Q. Wu, G.-Q. Liu, W.-H. Zhang and J. Jiang, *J. Phys. Chem. C*, 2019, **123**, 15996–16002.

8 P. Acharyya, T. Ghosh, K. Pal, K. Kundu, K. Singh Rana, J. Pandey, A. Soni, U. V. Waghmare and K. Biswas, *J. Am. Chem. Soc.*, 2020, **142**, 15595–15603.

9 H. Mishra, A. Bose, A. Dhar and S. Bhattacharya, *Phys. Rev. B*, 2018, **98**, 045143.

10 S. Shree, M. Semina, C. Robert, B. Han, T. Amand, A. Balocchi, M. Manca, E. Courtade, X. Marie, T. Taniguchi, K. Watanabe, M. M. Glazov and B. Urbaszek, *Phys. Rev. B*, 2018, **98**, 035302.

11 J. Nguepnang, C. Kenfack-Sadem, A. Kenfack-Jiotsa, C. Guimapi, A. Fotue and A. Merad, *Opt. Quantum Electron.*, 2021, **53**, 1–21.

12 S. D. Sarma and B. Mason, *Ann. Phys.*, 1985, **163**, 78–119.

13 T. Huang, K. Li, J. Lei, Q. Niu, H. Peng and B. Zou, *Nano Res.*, 2023, **16**, 12680–12688.

14 H. Luo, S. Guo, Y. Zhang, K. Bu, H. Lin, Y. Wang, Y. Yin, D. Zhang, S. Jin and W. Zhang, *et al.*, *Adv. Sci.*, 2021, **8**, 2100786.

15 W. Zhao, Z. Ma, Y. Shi, R. Fu, K. Wang, Y. Sui, G. Xiao and B. Zou, *Cell Rep. Phys. Sci.*, 2023, **4**, 101663.

16 C. Katan, N. Mercier and J. Even, *Chem. Rev.*, 2019, **119**, 3140–3192.

17 Z.-W. Wang, W.-P. Li, Y. Xiao, R.-Z. Li and Z.-Q. Li, *Appl. Phys. Lett.*, 2017, **110**, 101101.

18 K. Marjit, A. G. Francis, S. K. Pati and A. Patra, *J. Phys. Chem. Lett.*, 2023, **14**, 10900–10909.

19 P. Kaer and J. Mørk, *Phys. Rev. B: Condens. Matter Mater. Phys.*, 2014, **90**, 035312.

20 V. Quirós-Cordero, E. Rojas-Gatjens, M. Gómez-Dominguez, H. Li, C. A. Perini, N. Stingelin, E. R. Bittner, J.-P. Correa-Baena, A. R. S. Kandada and C. Silva-Acuña, *arXiv*, 2024, preprint, arXiv:2404.14744, DOI: **10.48550/arXiv.2404.14744**.

21 Y. Song, C. Qin, S. Dong, X. Li, A. Wei, G. Zhang, R. Chen, J. Hu, G. Zeng and L. Xiao, *et al.*, *Laser Photon. Rev.*, 2024, 2400093.

22 J. Fu, S. Ramesh, J. W. Melvin Lim and T. C. Sum, *Chem. Rev.*, 2023, **123**, 8154–8231.

23 S. Roche, J. Jiang, F. Triozon and R. Saito, *Phys. Rev. Lett.*, 2005, **95**, 076803.

24 L. Sun, P. Kumar, Z. Liu, J. Choi, B. Fang, S. Roesch, K. Tran, J. Casara, E. Priego and Y.-M. Chang, *et al.*, *Nano Lett.*, 2021, **21**, 1434–1439.

25 K. G. Nakamura and I. Takagi, *Progress in Ultrafast Intense Laser Science XVII*, Springer, 2024, pp. 101–118.

26 Q. Li, F. Liu, J. C. Russell, X. Roy and X. Zhu, *J. Chem. Phys.*, 2020, **152**, 124702.

27 L. R. Buizza and L. M. Herz, *Adv. Mater.*, 2021, **33**, 2007057.

28 J.-J. Shi, X.-Q. Zhu, Z.-X. Liu, S.-H. Pan and X.-Y. Li, *Phys. Rev. B: Condens. Matter Mater. Phys.*, 1997, **55**, 4670.

29 C. Franchini, M. Reticcioli, M. Setvin and U. Diebold, *Nat. Rev. Mater.*, 2021, **6**, 560–586.

23424 | *J. Mater. Chem. C*, 2025, **13**, 23416–23426

This journal is © The Royal Society of Chemistry 2025

30 G. Lanzani, G. Cerullo and S. De Silvestri, *Coherent Vibrational Dynamics*, CRC Press, 2007.

31 D. Emin, *Polarons*, Cambridge University Press, 2013.

32 D. Emin, *Phys. Rev. B: Condens. Matter Mater. Phys.*, 1993, **48**, 13691.

33 Y. Petrov, K. Migdal, N. Inogamov, V. Khokhlov, D. Ilnitsky, I. Milov, N. Medvedev, V. Lipp and V. Zhakhovsky, *Data Brief*, 2020, **28**, 104980.

34 V. Pipa, N. Vagidov, V. Mitin and M. Stroscio, *Phys. Rev. B: Condens. Matter Mater. Phys.*, 2001, **64**, 235322.

35 E. Tiras, S. Ardali, T. Tiras, E. Arslan, S. Cakmakyapan, O. Kazar, J. Hassan, E. JanzÈn and E. Ozbay, *J. Appl. Phys.*, 2013, **113**, 043708.

36 M. Manrho, T. L. Jansen and J. Knoester, *J. Chem. Phys.*, 2022, **156**, 224112.

37 A. Zaitsev, *Phys. Rev. B: Condens. Matter Mater. Phys.*, 2000, **61**, 12909.

38 V. Dzhagan, Y. M. Azhniuk, A. Milekhin and D. Zahn, *J. Phys. D: Appl. Phys.*, 2018, **51**, 503001.

39 L. Lüer, C. Gadermaier, J. Crochet, T. Hertel, D. Brida and G. Lanzani, *Phys. Rev. Lett.*, 2009, **102**, 127401.

40 D. A. Wheeler and J. Z. Zhang, *Adv. Mater.*, 2013, **25**, 2878–2896.

41 G. D. Scholes and G. Rumbles, *Nat. Mater.*, 2006, **5**, 683–696.

42 A. Burgos-Caminal, E. Socie, M. E. Bouduban and J.-E. Moser, *J. Phys. Chem. Lett.*, 2020, **11**, 7692–7701.

43 K. Miyata, D. Meggiolaro, M. T. Trinh, P. P. Joshi, E. Mosconi, S. C. Jones, F. De Angelis and X.-Y. Zhu, *Sci. Adv.*, 2017, **3**, e1701217.

44 D. Bao, Q. Chang, B. Chen, X. Chen, H. Sun, Y. M. Lam, D. Zhao, J.-X. Zhu and E. E. Chia, *PRX Energy*, 2023, **2**, 013001.

45 M. Puppin, S. Polishchuk, N. Colonna, A. Crepaldi, D. Dirin, O. Nazarenko, R. De Gennaro, G. Gatti, S. Roth and T. Barillot, *et al.*, *Phys. Rev. Lett.*, 2020, **124**, 206402.

46 R. Ghosh and F. C. Spano, *Acc. Chem. Res.*, 2020, **53**, 2201–2211.

47 F. C. Spano, *Acc. Chem. Res.*, 2010, **43**, 429–439.

48 A. S. Alexandrov, *Polarons in advanced materials*, Springer Science & Business Media, 2008, vol. 103.

49 Z.-G. Yu, Hybrid Organic Inorganic Perovskites. Physical Properties and Applications, *Hybrid Organic Inorganic Perovskites: Physical Properties*, 2022, vol. 1, pp. 195–239.

50 E. R. Powers, W. Paritmongkol, D. C. Yost, W. S. Lee, J. C. Grossman and W. A. Tisdale, *Matter*, 2024, **7**, 1612–1630.

51 L. Ni, U. Huynh, A. Cheminal, T. H. Thomas, R. Shivanna, T. F. Hinrichsen, S. Ahmad, A. Sadhanala and A. Rao, *ACS Nano*, 2017, **11**, 10834–10843.

52 W. Tao, Y. Zhang and H. Zhu, *Acc. Chem. Res.*, 2022, **55**, 345–353.

53 C. M. Mauck and W. A. Tisdale, *Trends Chem.*, 2019, **1**, 380–393.

54 H. Diab, G. Trippé-Allard, F. Lédée, K. Jemli, C. Vilar, G. Bouchez, V. L. Jacques, A. Tejeda, J. Even and J.-S. Lauret, *et al.*, *J. Phys. Chem. Lett.*, 2016, **7**, 5093–5100.

55 K. Gauthron, J. Lauret, L. Doyennette, G. Lanty, A. Al Choueiry, S. Zhang, A. Brehier, L. Largeau, O. Mauguin and J. Bloch, *et al.*, *Opt. Express*, 2010, **18**, 5912–5919.

56 J. Even, L. Pedesseau and C. Katan, *Chem. Phys. Chem.*, 2014, **15**, 3733–3741.

57 A. R. Srimath Kandada and C. Silva, *J. Phys. Chem. Lett.*, 2020, **11**, 3173–3184.

58 S. Biswas, R. Zhao, F. Alowa, M. Zacharias, S. Sharifzadeh, D. F. Coker, D. S. Seferos and G. D. Scholes, *Nat. Mater.*, 2024, 1–7.

59 F. Thouin, D. A. Valverde-Chávez, C. Quarti, D. Cortecchia, I. Bargigia, D. Beljonne, A. Petrozza, C. Silva and A. R. Srimath Kandada, *Nat. Mater.*, 2019, **18**, 349–356.

60 J. Fu, M. Li, A. Solanki, Q. Xu, Y. Lekina, S. Ramesh, Z. X. Shen and T. C. Sum, *Adv. Mater.*, 2021, **33**, 2006233.

61 J. Duan, J. Li, G. Divitini, D. Cortecchia, F. Yuan, J. You, S. Liu, A. Petrozza, Z. Wu and J. Xi, *Adv. Mater.*, 2024, **36**, 2403455.

62 N. Zhou and H. Zhou, *Samll Struct.*, 2022, **3**, 2100232.

63 Z. Ou, Y. J. Zheng, C. Li and K. Sun, *J. Phys. Chem. Lett.*, 2025, **16**, 802–810.

64 D. Ghosh, A. R. Smith, A. B. Walker and M. S. Islam, *Chem. Mater.*, 2018, **30**, 5194–5204.

65 S. Liu, R. Guo and F. Xie, *Mater. Des.*, 2022, **221**, 110951.

66 C. Wu, D. Guo, P. Li, S. Wang, A. Liu and F. Wu, *Phys. Chem. Chem. Phys.*, 2020, **22**, 3105–3111.

67 G. Giorgi, J.-I. Fujisawa, H. Segawa and K. Yamashita, *J. Phys. Chem. C*, 2014, **118**, 12176–12183.

68 S. Maheshwari, T. J. Savenije, N. Renaud and F. C. Grozema, *J. Phys. Chem. C*, 2018, **122**, 17118–17122.

69 N. Zibouche and M. S. Islam, *ACS Appl. Mater. Interfaces*, 2020, **12**, 15328–15337.

70 J. V. Passarelli, C. M. Mauck, S. W. Winslow, C. F. Perkinson, J. C. Bard, H. Sai, K. W. Williams, A. Narayanan, D. J. Fairfield and M. P. Hendricks, *et al.*, *Nat. Chem.*, 2020, **12**, 672–682.

71 D. B. Straus and C. R. Kagan, *J. Phys. Chem. Lett.*, 2018, **9**, 1434–1447.

72 Z. Ruan, S. Jiang and Q. Zhang, *J. Chem. Phys.*, 2023, **158**, 164706.

73 L. M. Herz, *J. Phys. Chem. Lett.*, 2018, **9**, 6853–6863.

74 F. Thouin, D. Cortecchia, A. Petrozza, A. R. Srimath Kandada and C. Silva, *Phys. Rev. Res.*, 2019, **1**, 032032.

75 F. Thouin, S. Neutzner, D. Cortecchia, V. A. Dragomir, C. Soci, T. Salim, Y. M. Lam, R. Leonelli, A. Petrozza and A. R. S. Kandada, *et al.*, *Phys. Rev. Mater.*, 2018, **2**, 034001.

76 D. B. Turner, K. W. Stone, K. Gundogdu and K. A. Nelson, *Rev. Sci. Instrum.*, 2011, **82**, 081301.

77 V. Loriot, G. Gitzinger and N. Forget, *Opt. Express*, 2013, **21**, 24879–24893.

78 E. I. Marchenko, V. V. Korolev, S. A. Fateev, A. Mitrofanov, N. N. Eremin, E. A. Goodilin and A. B. Tarasov, *Chem. Mater.*, 2021, **33**, 7518–7526.

79 J. A. Steele, E. Solano, D. Hardy, D. Dayton, D. Ladd, K. White, P. Chen, J. Hou, H. Huang and R. A. Saha, *et al.*, *Adv. Energy Mater.*, 2023, **13**, 2300760.

This journal is © The Royal Society of Chemistry 2025

J. Mater. Chem. C, 2025, **13**, 23416–23426 | 23425

80 N. E. Wright, X. Qin, J. Xu, L. L. Kelly, S. P. Harvey, M. F. Toney, V. Blum and A. D. Stiff-Roberts, *Chem. Mater.*, 2022, **34**, 3109–3122.

81 D. B. Straus, N. Iotov, M. R. Gau, Q. Zhao, P. J. Carroll and C. R. Kagan, *J. Phys. Chem. Lett.*, 2019, **10**, 1198–1205.

82 H.-H. Fang, J. Yang, S. Adjokatse, E. Tekelenburg, M. E. Kamminga, H. Duim, J. Ye, G. R. Blake, J. Even and M. A. Loi, *Adv. Funct. Mater.*, 2020, **30**, 1907979.

83 J. Yan, W. Zhang, S. Geng, C. Qiu, Y. Chu, R. Meng, P. Zeng, M. Liu, Z. Xiao and Y. Hu, *Chem. Mater.*, 2022, **35**, 289–294.

84 Y. Fu, X. Jiang, X. Li, B. Traore, I. Spanopoulos, C. Katan, J. Even, M. G. Kanatzidis and E. Harel, *J. Am. Chem. Soc.*, 2020, **142**, 4008–4021.

85 Y. Shao, W. Gao, H. Yan, R. Li, I. Abdelwahab, X. Chi, L. Rogée, L. Zhuang, W. Fu and S. P. Lau, *et al.*, *Nat. Commun.*, 2022, **13**, 138.

86 V. L. Cherrette, F. Babbe, J. K. Cooper and J. Z. Zhang, *J. Phys. Chem. Lett.*, 2023, **14**, 8717–8725.

87 S. Halder, M. S. Sheikh, B. Ghosh and T. Sinha, *Mater. Chem. Phys.*, 2017, **199**, 508–521.

88 P. C. Arpin, D. B. Turner, S. D. McClure, C. C. Jumper, T. Mirkovic, J. R. Challa, J. Lee, C. Y. Teng, B. R. Green and K. E. Wilk, *et al.*, *J. Phys. Chem. B*, 2015, **119**, 10025–10034.

89 C. C. Jumper, P. C. Arpin, D. B. Turner, S. D. McClure, S. R. Rather, J. C. Dean, J. A. Cina, P. A. Kovac, T. Mirkovic and G. D. Scholes, *J. Phys. Chem. Lett.*, 2016, **7**, 4722–4731.

90 P. J. Johnson, A. Halpin, T. Morizumi, L. S. Brown, V. I. Prokhorenko, O. P. Ernst and R. D. Miller, *Phys. Chem. Chem. Phys.*, 2014, **16**, 21310–21320.

91 D. Polli, P. Altoè, O. Weingart, K. M. Spillane, C. Manzoni, D. Brida, G. Tomasello, G. Orlandi, P. Kukura and R. A. Mathies, *et al.*, *Nature*, 2010, **467**, 440–443.

92 A. Kahan, O. Nahmias, N. Friedman, M. Sheves and S. Ruhman, *J. Am. Chem. Soc.*, 2007, **129**, 537–546.

93 M. H. Vos, F. Rappaport, J.-C. Lambry, J. Breton and J.-L. Martin, *Nature*, 1993, **363**, 320–325.

94 W. T. Pollard, S. L. Dexheimer, Q. Wang, L. A. Peteanu, C. V. Shank and R. A. Mathies, *J. Phys. Chem.*, 1992, **96**, 6147–6158.

95 S. D. McClure, D. B. Turner, P. C. Arpin, T. Mirkovic and G. D. Scholes, *J. Phys. Chem. B*, 2014, **118**, 1296–1308.

96 W. T. Pollard and R. A. Mathies, *Annu. Rev. Phys. Chem.*, 1992, **43**, 497–523.

97 S. Mukamel, *Principles of Nonlinear Optical Spectroscopy*, Oxford University Press, 1995.

98 A. T. Kumar, F. Rosca, A. Widom and P. M. Champion, *J. Chem. Phys.*, 2001, **114**, 701–724.

99 M. S. Barclay, J. S. Huff, R. D. Pensack, P. H. Davis, W. B. Knowlton, B. Yurke, J. C. Dean, P. C. Arpin and D. B. Turner, *J. Phys. Chem. Lett.*, 2022, **13**, 5413–5423.

100 D. B. Turner and P. C. Arpin, *Chem. Phys.*, 2020, **539**, 110948.

101 P. C. Arpin and D. B. Turner, *J. Phys. Chem. A*, 2021, **125**, 2425–2435.

102 M. Bauchy, M. Micoulaut, M. Celino, S. Le Roux, M. Boero and C. Massobrio, *Phys. Rev. B: Condens. Matter Mater. Phys.*, 2011, **84**, 054201.

103 W. H. Baur and R. X. Fischer, *Chem. Mater.*, 2019, **31**, 2401–2420.

104 E. Rojas-Gatjens, H. Li, A. Vega-Flick, D. Cortecchia, A. Petrozza, E. R. Bittner, A. R. Srimath Kandada and C. Silva-Acuña, *J. Phys. Chem. C*, 2023, **127**, 21194–21203.

105 A. R. Srimath Kandada, H. Li, E. R. Bittner and C. Silva-Acuña, *J. Phys. Chem. C*, 2022, **126**, 5378–5387.

106 D. Ghosh, E. Welch, A. J. Neukirch, A. Zakhidov and S. Tretiak, *J. Phys. Chem. Lett.*, 2020, **11**, 3271–3286.

107 M. Gomez-Dominguez, V. Quirós-Cordero, E. Rojas-Gatjens, K. A. Koch, E. J. Kumar, C. A. Perini, N. Stingelin, C. Silva-Acuña, A. R. Srimath Kandada and V. Menon, *et al.*, *ACS Photonics*, 2025, **12**, 2423–2431.

108 M. Dyksik, D. Beret, M. Baranowski, H. Duim, S. Moyano, K. Posmyk, A. Mlayah, S. Adjokatse, D. K. Maude and M. A. Loi, *et al.*, *Adv. Sci.*, 2024, **11**, 2305182.

23426 | *J. Mater. Chem. C*, 2025, **13**, 23416–23426

This journal is © The Royal Society of Chemistry 2025